Zheng et al. Nanoscale Research Letters (2017) 12:608
DOI 10.1186/s11671-017-2377-1

Nanoscale Research Letters

NANO COMMENTARY Open Access

A novel $Bi_4Ti_3O_{12}/Ag_3PO_4$ heterojunction photocatalyst with enhanced photocatalytic performance

Chengxiang Zheng[1,2], Hua Yang[1,2*], Ziming Cui[2], Haimin Zhang[2] and Xiangxian Wang[2]

Abstract

In this work, we integrated Ag_3PO_4 with $Bi_4Ti_3O_{12}$ to form $Bi_4Ti_3O_{12}/Ag_3PO_4$ heterojunction nanocomposites by an ion-exchange method. The as-prepared $Bi_4Ti_3O_{12}/Ag_3PO_4$ composites were systematically characterized by means of XRD, SEM, TEM, BET, XPS, UV-vis DRS, EIS, PL spectroscopy, and photocurrent response. SEM, TEM, and XPS results demonstrate the creation of $Bi_4Ti_3O_{12}/Ag_3PO_4$ heterojunction with obvious interfacial interaction between $Bi_4Ti_3O_{12}$ and Ag_3PO_4. PL spectra, EIS spectra, and photocurrent responses reveal that the composites display an enhanced separation efficiency of photogenerated electron-hole pairs, which is due to the charge transfer between $Bi_4Ti_3O_{12}$ and Ag_3PO_4. Rhodamine B (RhB) was chosen as the target organic pollutant to evaluate its degradation behavior over $Bi_4Ti_3O_{12}/Ag_3PO_4$ composites under simulated sunlight irradiation. Compared to bare $Bi_4Ti_3O_{12}$ and Ag_3PO_4 nanoparticles, the composites exhibit a significantly enhanced photocatalytic activity. The highest photocatalytic activity is observed for the 10% $Bi_4Ti_3O_{12}/Ag_3PO_4$ composite with 10% $Bi_4Ti_3O_{12}$ content, which is about 2.6 times higher than that of bare Ag_3PO_4. The photocatalytic mechanism involved was investigated and discussed in detail.

Keywords: $Bi_4Ti_3O_{12}$ nanoparticles, Ag_3PO_4 nanoparticles, $Bi_4Ti_3O_{12}/Ag_3PO_4$ heterojunction, Photocatalytic performance, Photocatalytic mechanism

Background

With the rapid development of economy, environmental pollution has become one of the most serious problems for human. Particularly, a huge amount of wastewater containing various organic dyes and pigments has been generated annually from chemical industries like paper, textile, paint, and cosmetic manufacturers all over the world. Before releasing the wastewater into the river, those organic pollutants must be removed since most of them are non-biodegradable and carcinogenic and pose an immense threat to the environment and human health. Semiconductor photocatalysis has been received as one of the most promising wastewater treatment technologies [1–9]. This technology can utilize solar energy as the power source for the organic pollutant decomposition. To utilize the solar energy more effectively in the photocatalysis, it is highly desirable to develop visible-light-responsive photocatalysts since visible light accounts for 45% of the solar energy. Moreover, to achieve a good photocatalytic activity of the photocatalyst, the photogenerated electron-hole (e^--h^+) pairs must be effectively separated because the photocatalytic reaction is associated with the photogenerated electrons and holes [10, 11].

Recently, silver orthophosphate (Ag_3PO_4) with a bandgap energy of ~ 2.4 eV has been extensively studied as a promising visible light photocatalyst [12–31]. First principle calculations based on the density functional theory suggested that Ag_3PO_4 has a highly dispersive band structure of the conduction band minimum resulting from Ag *s*-Ag *s* hybridization without localized *d* states [32], which is advantageous for the separation of electron hole pairs as well as the electron transfer. Furthermore, Ag_3PO_4 has a quantum efficiency much higher than the values reported for other semiconductors (~ 90% at $\lambda > 420$ nm) [12, 13]. These make Ag_3PO_4 an excellent photocatalytic activity for the decomposition of organic pollutants as well as O_2 evolution from water splitting under visible light irradiation.

* Correspondence: hyang@lut.cn
[1]State Key Laboratory of Advanced Processing and Recycling of Non-ferrous Metals, Lanzhou University of Technology, Lanzhou 730050, China
[2]School of Science, Lanzhou University of Technology, Lanzhou 730050, China

However, there are still some limitations in the Ag_3PO_4 photocatalyst. It is noted that the conduction band potential of Ag_3PO_4 is more positive than that of the hydrogen electrode [12]. This means that if there are no sacrificial electron acceptors involved in the photocatalytic system, the photogenerated electrons could reduce the lattice Ag^+ in Ag_3PO_4 into metallic Ag during the photocatalytic process. This self-photocorrosive phenomenon leads to a decrease in the photocatalytic stability of Ag_3PO_4. Moreover, Ag_3PO_4 is slightly soluble in aqueous solution, which could also decrease its structural stability during the photocatalytic process. To further improve the photocatalytic performance as well as the photocatalytic stability of Ag_3PO_4, much recent work has been devoted to the heterojunction composites constructed from Ag_3PO_4 and other semiconductors, such as AgX/Ag_3PO_4 (X = Cl, Br, I), Fe_3O_4/Ag_3PO_4, Ag_3PO_4/SnO_2, Ag_3PO_4/TiO_2, Ag_3PO_4/Bi_2MoO_6, $g\text{-}C_3N_4/Ag_3PO_4$, Ag_3PO_4/CeO_2, $Ag_3PO_4/SrTiO_3$, $Ag_3PO_4/BiPO_4$, Ag_3PO_4/MoS_2, and $Ag_3PO_4/g\text{-}C_3N_4$ [33–46]. In these composite photocatalysts, photogenerated electrons and holes tend to migrate from one semiconductor to another, leading to an efficient separation of electron hole pairs. As a result, more photogenerated electrons and/or holes are available for participating in photocatalytic reactions. It has been shown that the heterojunction composites exhibit enhanced photocatalytic performance compared to individual semiconductors. Furthermore, the photocorrosion and solubility behaviors of Ag_3PO_4 can be inhibited to some extent by the construction of heterojunction composites.

In this work, we report the integration of Ag_3PO_4 with $Bi_4Ti_3O_{12}$ to form $Ag_3PO_4/Bi_4Ti_3O_{12}$ heterojunction composites. $Bi_4Ti_3O_{12}$ has a layered structure composed of alternate $(Bi_2Ti_3O_{10})^{2-}$ blocks and $(Bi_2O_2)^{2+}$ layers along the *c*-axis orientation [47]. Density functional theory calculation has shown that the conduction band (CB) and valence band (VB) of $Bi_4Ti_3O_{12}$ consist of Ti 3d + Bi 6p orbitals and O 2p + Bi 6 s hybrid orbitals, respectively [48]. Due to its unique layered crystal structure and electronic band structure, $Bi_4Ti_3O_{12}$ exhibits pronounced photocatalytic activity toward the degradation of organic pollutants [49–53]. It is known that Ag_3PO_4 is a p-type semiconductor and $Bi_4Ti_3O_{12}$ is an n-type semiconductor. The well-matched overlapping band-structures suggest that Ag_3PO_4 and $Bi_4Ti_3O_{12}$ can be used to construct an excellent p-n heterojunction composite photocatalyst with super photocatalytic performance.

Methods

Synthesis of $Bi_4Ti_3O_{12}$ and Ag_3PO_4 nanoparticles

$Bi_4Ti_3O_{12}$ nanoparticles were synthesized via a polyacrylamide gel route as described in the literature [54]. All raw materials and chemical reagents were of analytical grade and were used without further purification. Five milligrams of HNO_3 was added to 20 mL distilled water to make a dilute nitric acid solution. 0.00857 mol of $Bi(NO_3)_3{\cdot}5H_2O$ was dissolved in the above dilute nitric acid solution (designated as solution A). 0.00643 mol of $C_{16}H_{36}O_4Ti$ was dissolved in 25 mL ethanol (designated as solution B). The solution B was added slowly into the solution A to obtain a mixture solution. Then, the mixture solution were successively added with 0.0225 mol of citric acid, 20 g of glucose, and 0.135 mol of acrylamide. During the addition of chemical reagents, the solution was agitated by magnetic stirring to make the additives dissolve fully. The resultant solution was heated in a water bath at 80 °C to initiate the polymerization reaction. After dried at 120 °C for 24 h in a thermostat drier, the formed xerogel was ground into powder and submitted to calcination in a tubular furnace at 300 °C for 3 h and then at 500 °C for 8 h. After the tubular furnace was naturally cooled down to room temperature, $Bi_4Ti_3O_{12}$ nanoparticles were obtained.

Ag_3PO_4 nanoparticles were synthesized by an ion exchange method. 0.003 mol of $AgNO_3$ and 0.001 mol of Na_2HPO_4 were dissolved in 30 and 20 mL distilled water with the aid of magnetic stirring, respectively. The Na_2HPO_4 solution was added drop by drop to the $AgNO_3$ solution under continuous stirring. The mixture solution was then continuously stirred by a magnetic stirrer for 5 h, during which time Ag_3PO_4 nanoparticles were formed. The produced particles were collected and washed several times with distilled water and absolute ethanol, followed by drying at 60 °C for 10 h.

Preparation of $Bi_4Ti_3O_{12}/Ag_3PO_4$ nanocomposites

A stoichiometric amount of the as-prepared $Bi_4Ti_3O_{12}$ nanoparticles was added to 30 mL distilled water and was submitted to ultrasonic treatment for 1 h to make the particles disperse uniformly. To the suspension was dissolved 0.003 mol of $AgNO_3$. 0.001 mol of Na_2HPO_4 was dissolved in 20 mL distilled water, which was then added drop by drop to the above suspension. The resultant mixture solution was magnetically stirred for 5 h, during which time Ag_3PO_4 nanoparticles were grown and integrated with $Bi_4Ti_3O_{12}$ nanoparticles to form $Bi_4Ti_3O_{12}/Ag_3PO_4$ composites. The produced composites were collected, washed several times with distilled water and absolute ethanol, and dried at 60 °C for 10 h. By varying the $Bi_4Ti_3O_{12}$ content from 5 to 15%, several composite samples of 5% $Bi_4Ti_3O_{12}/Ag_3PO_4$, 10% $Bi_4Ti_3O_{12}/Ag_3PO_4$, and 15% $Bi_4Ti_3O_{12}/Ag_3PO_4$ were prepared.

Sample characterization

X-ray powder diffraction (XRD) with Cu Kα radiation was used to determine the crystal structure of the samples. Field emission scanning electron microscopy (SEM) and field emission transmission electron microscopy (TEM)

were used to investigate the morphology and microstructure of the samples. The optical absorption and bandgap energy of the samples was investigated by ultraviolet-visible diffuse reflectance spectroscopy (UV-vis DRS) on a UV-vis spectrophotometer with an integrating sphere attachment. The chemical composition and electron binding energies for the elements were measured by X-ray photoelectron spectroscopy (XPS) on a PHI-5702 multifunctional X-ray photoelectron spectrometer, where the binding energy scale of the XPS data was calibrated against the adventitious C 1s peak at the binding energy of 284.8 eV. The photoluminescence (PL) spectrum of the samples was measured by using a fluorescence spectrophotometer (excitation wavelength 315 nm).

Photoelectrochemical measurement

The photoelectrochemical properties of the photocatalysts were measured by electrochemical impedance spectroscopy (EIS) and photocurrent response on a CST 350 electrochemical workstation using a three-electrode cell configuration [55]. A platinum foil was used as the counter electrode, and a standard calomel electrode (SCE) was used as the reference electrode. The working electrode was prepared as follows: 15 mg of the photocatalysts and 0.75 mg of polyvinylidene fluoride (PVDF) were mixed together using 1-methyl-2-pyrrolidione (NMP) as solvent to form slurry. The slurry was uniformly coated onto fluorine-doped tin oxide (FTO) glass substrate with an area of 1 cm × 1 cm and then submitted to drying at 60 °C for 5 h in a thermostat drying oven. Na_2SO_4 aqueous solution with concentration of 0.1 mol L^{-1} was used as the electrolyte. The EIS measurement was carried out by the use of the sinusoidal voltage pulse with amplitude of 5 mV and in the frequency range of 10^{-2}– 10^{5} Hz. The transient photocurrent response was measured at a bias potential of 0.2 V. During the photoelectrochemical measurements, the working electrode was irradiated by a 200 W xenon lamp.

Photocatalytic evaluation

Rhodamine B (RhB) was chosen as the target organic pollutant to evaluate its degradation behavior over the samples under irradiation from a 200 W xenon lamp (solar simulator). RhB was dissolved in distilled water to make 5 mg L^{-1} RhB aqueous solution. Twenty milligrams of the photocatalyst was loaded in 100 mL of RhB solution. The mixed suspension was firstly stirred by a magnetic stirrer for 20 min in the dark and then submitted to photocatalysis. During the photocatalysis process, the reactor was cooled with a water cooling system to maintain the reaction solution at room temperature. At given time intervals, a small portion of the reaction solution was taken out from the reactor for examining the RhB concentration, which was determined by measuring the absorbance of the solution at $\lambda = 554$ nm on a UV-vis spectrophotometer. Before absorbance measurement, the photocatalyst was removed by centrifugalization. The percentage degradation of RhB is defined as $(C_0 - C_t)/C_0 \times 100\%$, where C_0 is the initial RhB concentration and C_t is the remaining RhB concentration after photocatalysis for time t.

Detection of hydroxyl

PL spectroscopy is an important technique that can be used to detect hydroxyl (•OH) radicals formed over the simulated sunlight irradiated photocatalyst. Here, terephthalic acid (TPA) was used as the •OH scavenger to examine •OH radicals. NaOH solution with concentration of 1.0 mmol L^{-1} was prepared by dissolving NaOH in distilled water. A stoichiometric amount of TPA was dissolved in the above NaOH solution to make 0.25 mmol L^{-1} TPA solution. Twenty milligrams of the photocatalyst was loaded in 100 mL of the TPA solution. The mixture was magnetically stirred for 20 min in the dark and then irradiated by a 200-W xenon lamp. A small portion of the solution was taken out from the reactor after reaction for a certain period of time and submitted to centrifugation to remove the photocatalyst. The PL spectrum of the clear solution was measured on a fluorescence spectrophotometer (excitation wavelength 315 nm).

Results and discussion

XRD analysis

Figure 1 shows the XRD patterns of $Bi_4Ti_3O_{12}$, Ag_3PO_4, 5% $Bi_4Ti_3O_{12}/Ag_3PO_4$, 10% $Bi_4Ti_3O_{12}/Ag_3PO_4$, and 15% $Bi_4Ti_3O_{12}/Ag_3PO_4$ samples. The standard XRD line patterns for $Bi_4Ti_3O_{12}$ orthorhombic structure (JCPDS card no. 035-0795) and Ag_3PO_4 cubic structure (JCPDS card no. 006-0505) are also shown in Fig. 1. For $Bi_4Ti_3O_{12}$ sample, all diffraction peaks are in good agreement with those in the JCPDS card no. 035-0795, indicating that the sample crystallizes in a pure $Bi_4Ti_3O_{12}$ orthorhombic phase [54]. For Ag_3PO_4 sample, all diffraction peaks can be indexed according to the standard diffraction lines in the JCPDS card no. 006-0505, implying the formation of pure Ag_3PO_4 cubic phase [31]. For the composites, the XRD patterns can be indexed into two sets of diffraction peaks corresponding to $Bi_4Ti_3O_{12}$ and Ag_3PO_4 phases. The peak intensity from $Bi_4Ti_3O_{12}$ phase increases with increasing its content, which is clearly seen from the $Bi_4Ti_3O_{12}$ (171) diffraction peak at 30.1°. No diffraction peaks assignable to other impurity phases are detected, indicating that $Bi_4Ti_3O_{12}$ and Ag_3PO_4 undergo no structural change in the composites.

SEM analysis

Figure 2a–c shows the SEM images of Ag_3PO_4, $Bi_4Ti_3O_{12}$, and 10% $Bi_4Ti_3O_{12}/Ag_3PO_4$ samples, respectively. The SEM image given in Fig. 2a shows that the

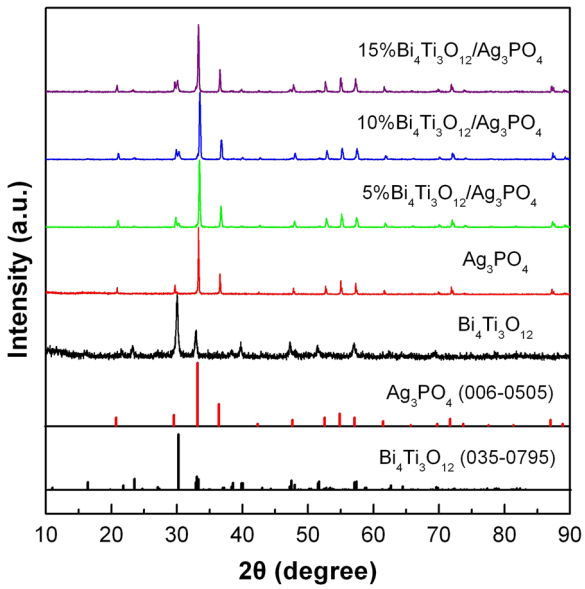

Fig. 1 XRD patterns of $Bi_4Ti_3O_{12}$, Ag_3PO_4, and $Bi_4Ti_3O_{12}/Ag_3PO_4$ composites

Ag_3PO_4 particles have sphere-like morphology with size ranging from 300 to 600 nm. The SEM image shown in Fig. 2b reveals that the $Bi_4Ti_3O_{12}$ particles present sphere-like or ellipsoid-like morphology and have a size distribution range of 60–90 nm. From the SEM image in Fig. 2c, one can see that small-sized $Bi_4Ti_3O_{12}$ particles are assembled onto the surface of large-sized Ag_3PO_4 particles to form $Bi_4Ti_3O_{12}/Ag_3PO_4$ heterostructure, as indicated by arrows.

TEM analysis

TEM was used to further investigate the microstructure of $Bi_4Ti_3O_{12}/Ag_3PO_4$ composites. Figure 3a shows the TEM image of 10% $Bi_4Ti_3O_{12}/Ag_3PO_4$. The large-sized particles are identified to be Ag_3PO_4 particles, which have a spherical morphology with size of several hundred nanometers. Much smaller-sized particles with diameter of several tens of nanometers, which are identified to be $Bi_4Ti_3O_{12}$ nanoparticles, are seen to be assembled onto Ag_3PO_4 particles, as indicated by arrows. The TEM observation indicates the formation of $Bi_4Ti_3O_{12}/Ag_3PO_4$ heterostructure, which agrees with that observed from the SEM image. Figure 3b shows the dark field scanning TEM (DF-STEM) image of 10% $Bi_4Ti_3O_{12}/Ag_3PO_4$. The corresponding elemental mapping images of the region indicated in Fig. 3b are given in Fig. 3c–g. It is seen that the large-sized particles present the elemental distribution of Ag and P and are therefore confirmed to be Ag_3PO_4 particles. The small-sized particles anchored onto Ag_3PO_4 particles display the elemental distribution of Bi and Ti, confirming that they are $Bi_4Ti_3O_{12}$ particles. The elemental mapping images further reveal the integration of $Bi_4Ti_3O_{12}$ with Ag_3PO_4 to form $Bi_4Ti_3O_{12}/Ag_3PO_4$ heterostructure. Furthermore, the elements Ag and P, as

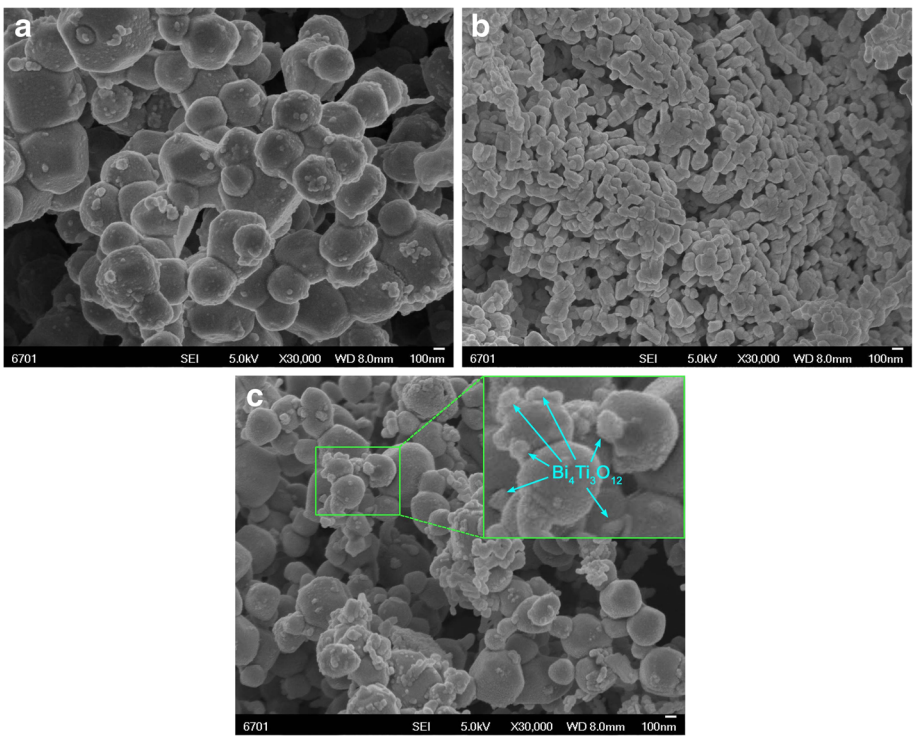

Fig. 2 SEM images of **a** Ag_3PO_4, **b** $Bi_4Ti_3O_{12}$, and **c** 10%$Bi_4Ti_3O_{12}/Ag_3PO_4$

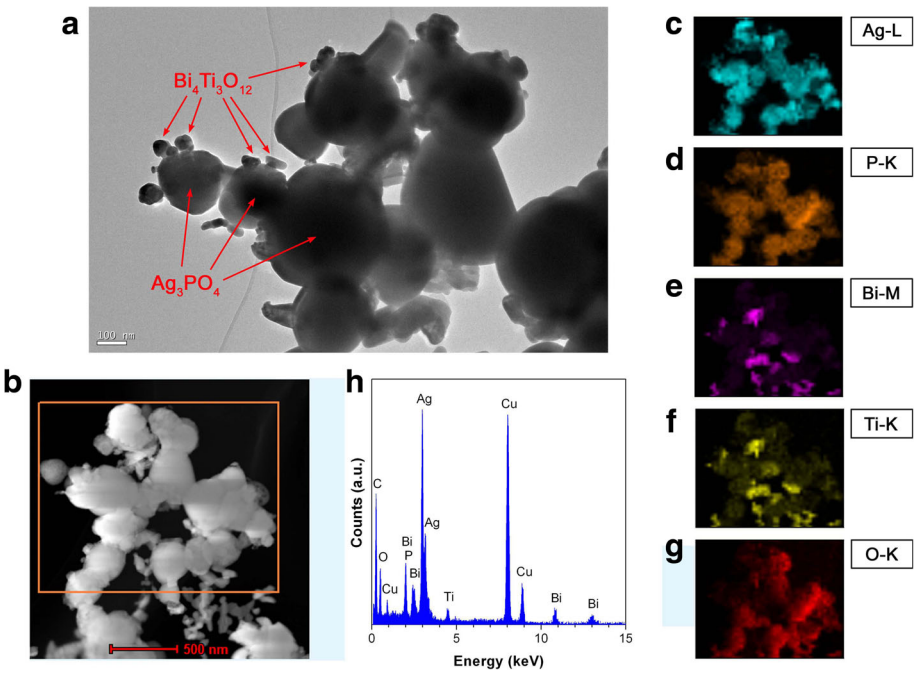

Fig. 3 **a** TEM image of 10% $Bi_4Ti_3O_{12}/Ag_3PO_4$. **b** DF-STEM image of 10% $Bi_4Ti_3O_{12}/Ag_3PO_4$. **c**–**g** The corresponding elemental mapping images of the region indicated in **b**. **h** EDS spectrum of 10% $Bi_4Ti_3O_{12}/Ag_3PO_4$

well as Bi and Ti, have an identical distribution, implying no chemical composition segregation in the Ag_3PO_4 and $Bi_4Ti_3O_{12}$ phases. The O element distribution is observed through the whole composites. Energy-dispersive X-ray spectroscopy (EDS) was further used to analyze the chemical composition of 10% $Bi_4Ti_3O_{12}/Ag_3PO_4$. As shown in Fig. 3h, the signals of the constituent elements of the composite are clearly included in the spectrum. The observed C and Cu signals could derive from the microgrid that is used for supporting the sample. It is noted that EDS is suitably used for the quantitative determination of the content of heavy elements (e.g., Bi, Ti, and Ag), but not light elements (e.g., P and O) [56]. The atomic ratio of Bi to Ti is obtained as 4/3 from the EDS spectrum, which agrees well the Bi/Ti atomic ratio of $Bi_4Ti_3O_{12}$ phase. The atomic ratio of Ti/Ag is very close to 1/9, implying that $Bi_4Ti_3O_{12}$ phase accounts for about 10% of the total molar content of the composite.

BET surface analysis

Figure 4 shows the N_2 adsorption-desorption isotherm of 10% $Bi_4Ti_3O_{12}/Ag_3PO_4$. This kind of isotherm is very similar to type II adsorption isotherm according to the IUPAC classification. The desorption curve coincides almost with the adsorption curve with no obvious hysteresis loop, implying the absence of mesopores in the composite. The insert in Fig. 4 shows the Brunauer-Emmett-Teller (BET) surface area plot of the composite, from which the BET surface area is calculated to be 2.08 $m^2\ g^{-1}$.

XPS analysis

The chemical composition and elemental oxidation state of Ag_3PO_4, $Bi_4Ti_3O_{12}$, and 10% $Bi_4Ti_3O_{12}/Ag_3PO_4$ were also investigated by XPS. Figure 5a shows the XPS survey scan spectra of the samples, revealing that the samples clearly include their own constituent elements and no other impurity elements are found. Figure 5b shows the O 1s XPS spectra of the samples. For bare

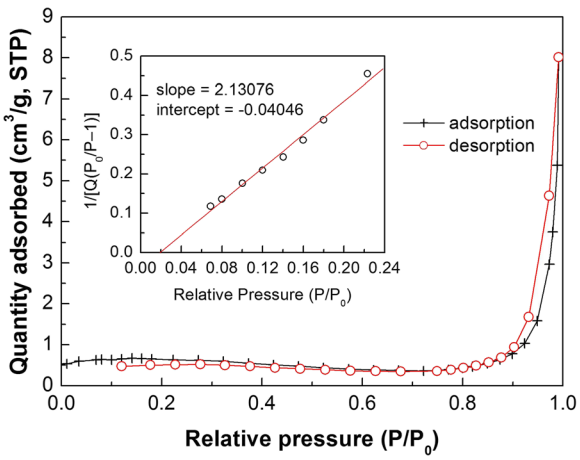

Fig. 4 N_2 adsorption-desorption isotherm and BET surface area plot of 10% $Bi_4Ti_3O_{12}/Ag_3PO_4$

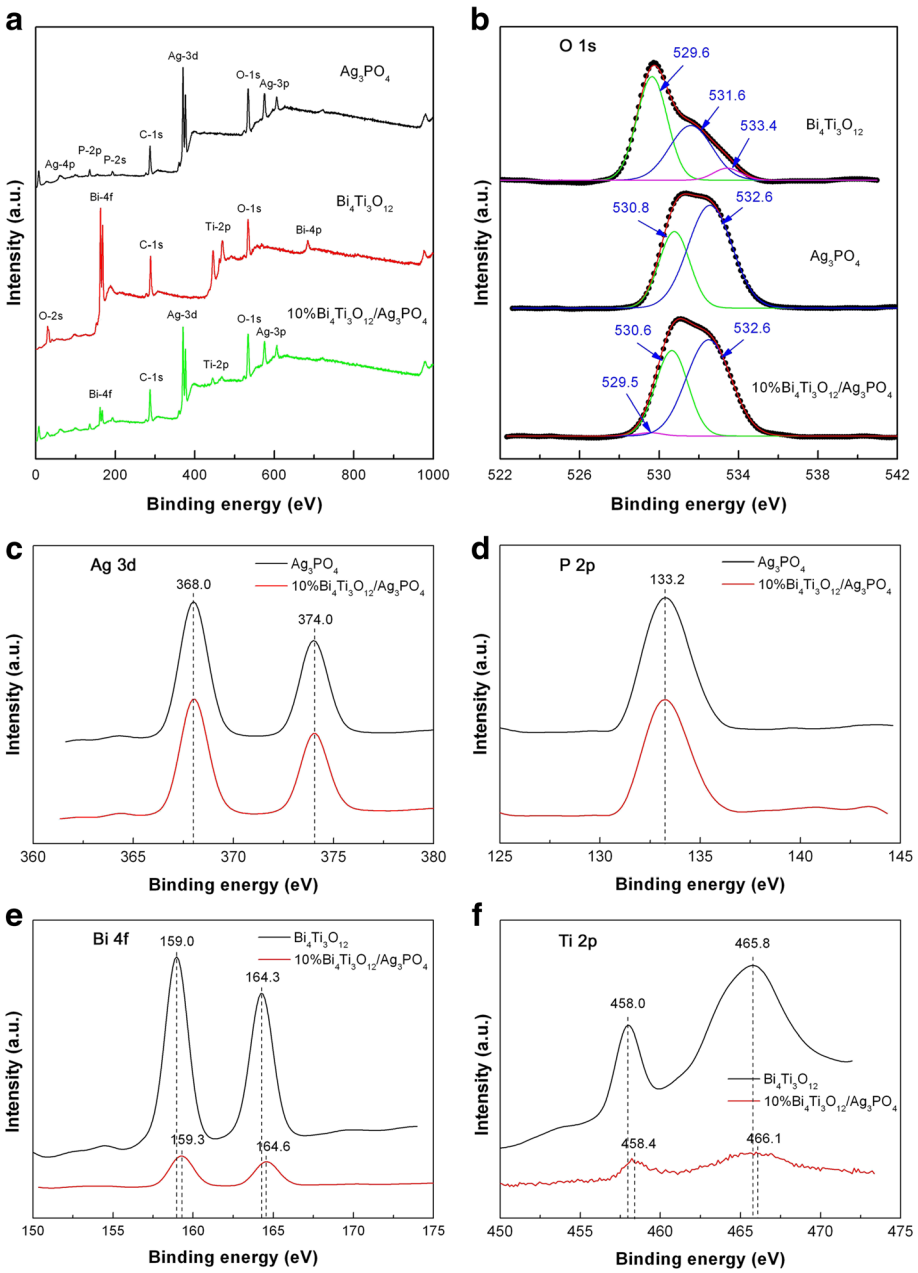

Fig. 5 XPS spectra of $Bi_4Ti_3O_{12}$, Ag_3PO_4, and 10% $Bi_4Ti_3O_{12}/Ag_3PO_4$. **a** XPS survey scan spectra. **b** O 1s XPS spectra. **c** Ag 3d XPS spectra. **d** P 2p XPS spectra. **e** Bi 4f XPS spectra. **f** Ti 2p XPS spectra

$Bi_4Ti_3O_{12}$, the O 1s XPS signal can be fitted into three peaks at 529.6, 531.6, and 533.4 eV. The binding energy at 529.6 eV is attributed to the contribution of the crystal lattice oxygen. The peaks at higher binding energies of 531.6 and 533.4 eV could arise due to surface defects and chemisorbed oxygen species [55]. For bare Ag_3PO_4, the O 1s XPS spectrum is deconvoluted into two peaks at 530.8 and 532.6 eV, which are ascribed to the crystal lattice oxygen and the surface adsorbed oxygen, respectively. For 10% $Bi_4Ti_3O_{12}/Ag_3PO_4$, the O 1s binding energy of the crystal lattice oxygen in $Bi_4Ti_3O_{12}$ and Ag_3PO_4 is observed at 529.5 and 530.6 eV, respectively. A slight downshift of the O 1s binding energy peaks is observed in the composite, implying the possible chemical bonding between $Bi_4Ti_3O_{12}$ and Ag_3PO_4. Figure 5c, d shows the XPS spectra of Ag 3d and P 2p, respectively. The peaks at 368.0 and 374.0 eV belong to the binding energies for Ag $3d_{5/2}$ and Ag $3d_{3/2}$, respectively, suggesting the presence of Ag^+ oxidation state. The presence of Ag^0 metal state in the samples can be excluded because no

additional peaks are visible on the Ag 3d XPS spectra [37]. The observation of the P 2p binding energy at 133.2 eV is indicative of the presence of P^{5+} oxidation state [37]. The Ag 3d and P 2p XPS signals undergo no change in the composite. Figure 5e, f shows the XPS spectra of Bi 4f and Ti 2p, respectively. For bare $Bi_4Ti_3O_{12}$, the Bi 4f spectrum presents two sharp peaks at 159.0 and 164.3 eV, which correspond to the binding energies of Bi $4f_{7/2}$ and Bi $4f_{5/2}$, respectively [52]. This implies that Bi exists in the + 3 oxidation state. On the Ti 2p spectrum, the peaks at 458.0 and 465.8 eV are assigned to the binding energies for Ti $2p_{3/2}$ and Ti $2p_{1/2}$, respectively, which indicates that Ti is in the form of Ti^{4+} oxidation state [52]. For the composite, the Bi 4f and Ti 2p peaks exhibit a slight shift toward higher binding energies, which could arise due to the chemical bonding between $Bi_4Ti_3O_{12}$ and Ag_3PO_4.

UV-vis DRS spectra

Figure 6a shows the UV-vis DRS spectra of $Bi_4Ti_3O_{12}$, Ag_3PO_4, and $Bi_4Ti_3O_{12}/Ag_3PO_4$ composites, and Fig. 6b gives the corresponding first derivative of the spectra. The absorption edge of the samples can be derived from the peaks on the first derivative spectra. It is seen that $Bi_4Ti_3O_{12}$ has an absorption edge at 376.9 nm, and Ag_3PO_4 has an absorption edge at 498.5 nm. The absorption edges arise due to the electron transition from the valence band to the conduction band of the semiconductors, from which the bandgap energies (E_g) of $Bi_4Ti_3O_{12}$ and Ag_3PO_4 are obtained to be 3.29 and 2.49 eV, respectively. For the composites, the absorption edges of $Bi_4Ti_3O_{12}$ and Ag_3PO_4 exhibit a slight shift toward the short wavelength, which could be due to their mutual effect of light absorption on each other. The bandgap energies of $Bi_4Ti_3O_{12}$ and Ag_3PO_4 are expected to undergo a negligible change in the composites.

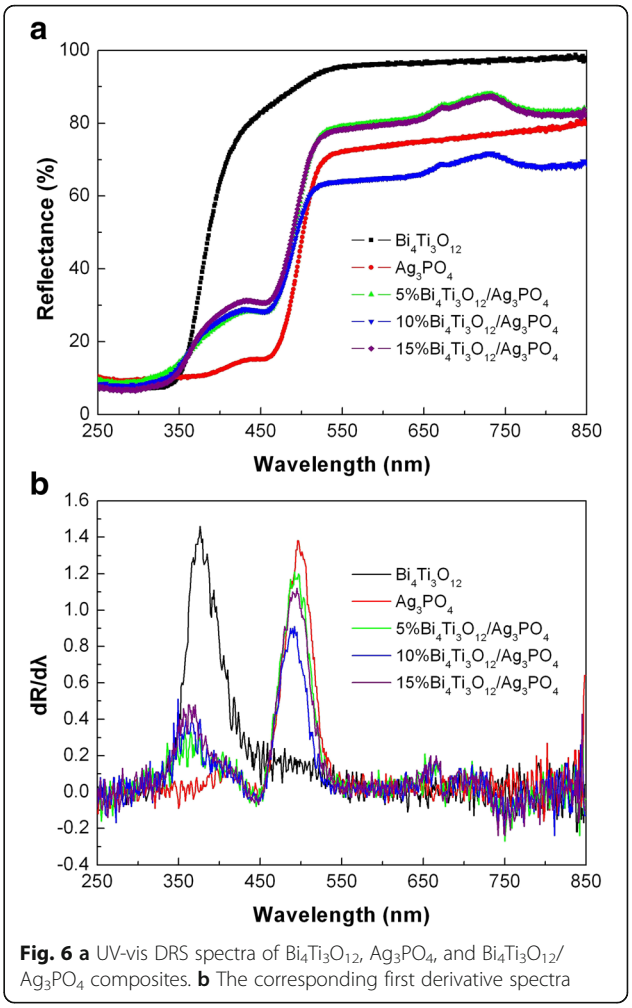

Fig. 6 **a** UV-vis DRS spectra of $Bi_4Ti_3O_{12}$, Ag_3PO_4, and $Bi_4Ti_3O_{12}/Ag_3PO_4$ composites. **b** The corresponding first derivative spectra

PL spectra

PL spectroscopy is used to evaluate the recombination behavior of photogenerated electron-hole pairs in the photocatalysts. The PL intensity is in proportion to the recombination rate of photogenerated electrons and holes. Figure 7 shows the PL spectra of Ag_3PO_4 and 10% $Bi_4Ti_3O_{12}/Ag_3PO_4$ measured at an excitation wavelength of 315 nm. For Ag_3PO_4 particles, three PL emission peaks are observed at around 430, 490, and 525 nm. In contrast, the intensity of the PL emission peaks from 10% $Bi_4Ti_3O_{12}/Ag_3PO_4$ composite is clearly decreased, implying a decrease in the electron-hole recombination. The efficient separation of electron-hole pairs is attributed to the charge transfer between $Bi_4Ti_3O_{12}$ and Ag_3PO_4. As a result, photogenerated electrons and holes in $Bi_4Ti_3O_{12}/Ag_3PO_4$ composites are increasingly available for the photocatalytic reactions.

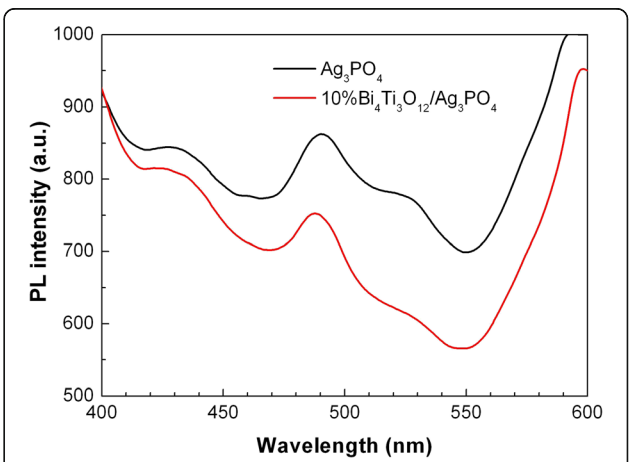

Fig. 7 PL spectra of Ag_3PO_4 and 10% $Bi_4Ti_3O_{12}/Ag_3PO_4$

Photoelectrochemical properties

EIS and photocurrent response can be also used to investigate the separation and transfer behavior of photogenerated electrons and holes in the photocatalysts. Figure 8a shows the Nyquist plots of the EIS spectra for Ag_3PO_4 and 10% $Bi_4Ti_3O_{12}/Ag_3PO_4$ electrodes, which present a typical semicircle. The diameter of the semicircle is related to the charge-transfer resistance at the electrode/electrolyte interface. It is obvious that the Nyquist plot of 10% $Bi_4Ti_3O_{12}/Ag_3PO_4$ shows a much smaller semicircle diameter than that of bare Ag_3PO_4, indicating that the composite has a relatively smaller charge-transfer resistance under simulated sunlight irradiation. The observation of smaller charge-transfer resistance implies an increased separation efficiency of photogenerated electron-hole pairs and fast interface charge transfer occurring in the 10% $Bi_4Ti_3O_{12}/Ag_3PO_4$ composite. Figure 8b shows the transient photocurrent responses of Ag_3PO_4 and 10%$Bi_4Ti_3O_{12}/Ag_3PO_4$ recorded for several switch-on and switch-off cycles under intermittent irradiation of simulated sunlight. It is seen that the transient photocurrent responses are highly reproducible when the light is repeatedly switched between on and off. During the irradiation period, the photocurrent density of 10% $Bi_4Ti_3O_{12}/Ag_3PO_4$ is obtained as ~ 24 μA cm^{-2}, which is much higher than that of bare Ag_3PO_4 (~ 4 μA cm^{-2}), indicating a more efficient separation of photogenerated electron-hole pairs in the composite due to the carrier transfer between $Bi_4Ti_3O_{12}$ and Ag_3PO_4.

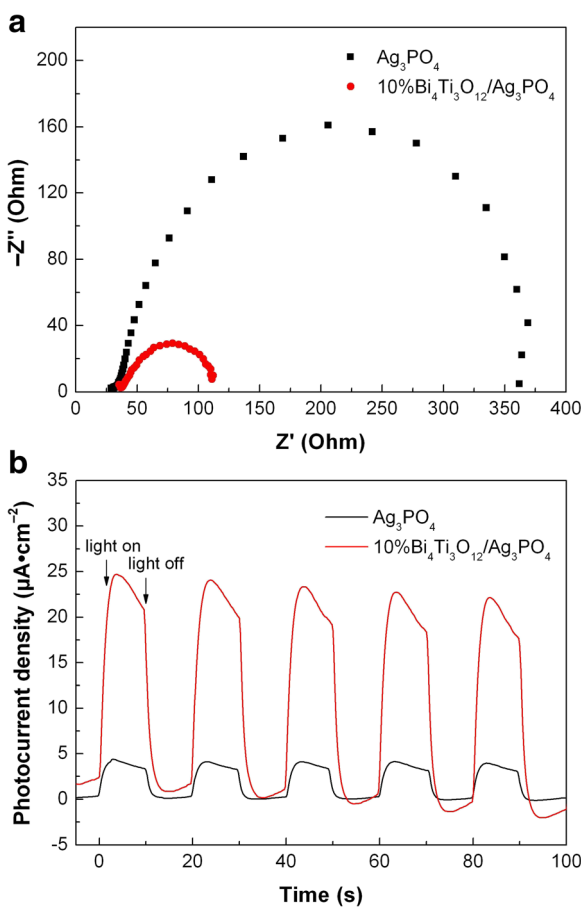

Fig. 8 **a** Nyquist plots of the EIS spectra for Ag_3PO_4 and 10% $Bi_4Ti_3O_{12}/Ag_3PO_4$. **b** Transient photocurrent responses of Ag_3PO_4 and 10% $Bi_4Ti_3O_{12}/Ag_3PO_4$

Photocatalytic performances

Figure 9a shows the time-dependent photocatalytic degradation of RhB over $Bi_4Ti_3O_{12}$, Ag_3PO_4, and $Bi_4Ti_3O_{12}/Ag_3PO_4$ composites under simulated sunlight irradiation, along with the blank experiment result. Without loading the photocatalyst, RhB exhibits a good stability under simulated sunlight irradiation and its percentage degradation is only about 1.7% after 30 min of irradiation. When Ag_3PO_4 is used as the photocatalyst, RhB undergoes a substantial degradation with increasing the irradiation time, while a relatively weak degradation of the dye is observed for $Bi_4Ti_3O_{12}$. More importantly, when Ag_3PO_4 is integrated with $Bi_4Ti_3O_{12}$, the formed $Bi_4Ti_3O_{12}/Ag_3PO_4$ heterojunction composites exhibit significantly enhanced photocatalytic activity compared to bare Ag_3PO_4 or $Bi_4Ti_3O_{12}$. The highest photocatalytic activity is observed for 10% $Bi_4Ti_3O_{12}/Ag_3PO_4$, where the percentage degradation of RhB after 30 min of photocatalysis reaches 99.5%, as shown in Fig. 9c. To further reveal the photocatalytic activity of the samples, the photocatalytic degradation kinetics of RhB is investigated. Figure 9b shows the plots of $\mathrm{Ln}(C_t/C_0)$ versus irradiation time (t) for the samples. It is seen that the dye degradation conforms well to the first-order kinetic equation $\mathrm{Ln}(C_t/C_0) = -k_{app}t$, where k_{app} is the apparent first-order reaction rate constant (min^{-1}) [57]. The obtained rate constants for the samples are shown in Fig. 9d. The rate constant k_{app} for 10% $Bi_4Ti_3O_{12}/Ag_3PO_4$ is obtained as 0.17891 min^{-1}, compared to 0.06764 min^{-1} for Ag_3PO_4. This implies that the photocatalytic activity of 10% $Bi_4Ti_3O_{12}/Ag_3PO_4$ is about 2.6 times higher than that of bare Ag_3PO_4.

In most of the photocatalytic systems, the dominant active species responsible for the dye degradation include •OH, superoxide ($\bullet O_2^-$), and h^+ [58]. It is known that •OH, $\bullet O_2^-$, and h^+ can be scavenged by ethanol, benzoquinone (BQ), and ammonium oxalate (AO), respectively [56]. Therefore, the role of the active species in the photocatalysis can be verified by investigating the effect of ethanol, BQ, and AO on the photocatalytic degradation of the dye. Five milligrams of ethanol, 0.0011 g of BQ, and 0.0142 g of AO are separately added in 100 mL reaction solution, and then, the photocatalytic experiments are carried out under the same conditions. Figure 10a shows the

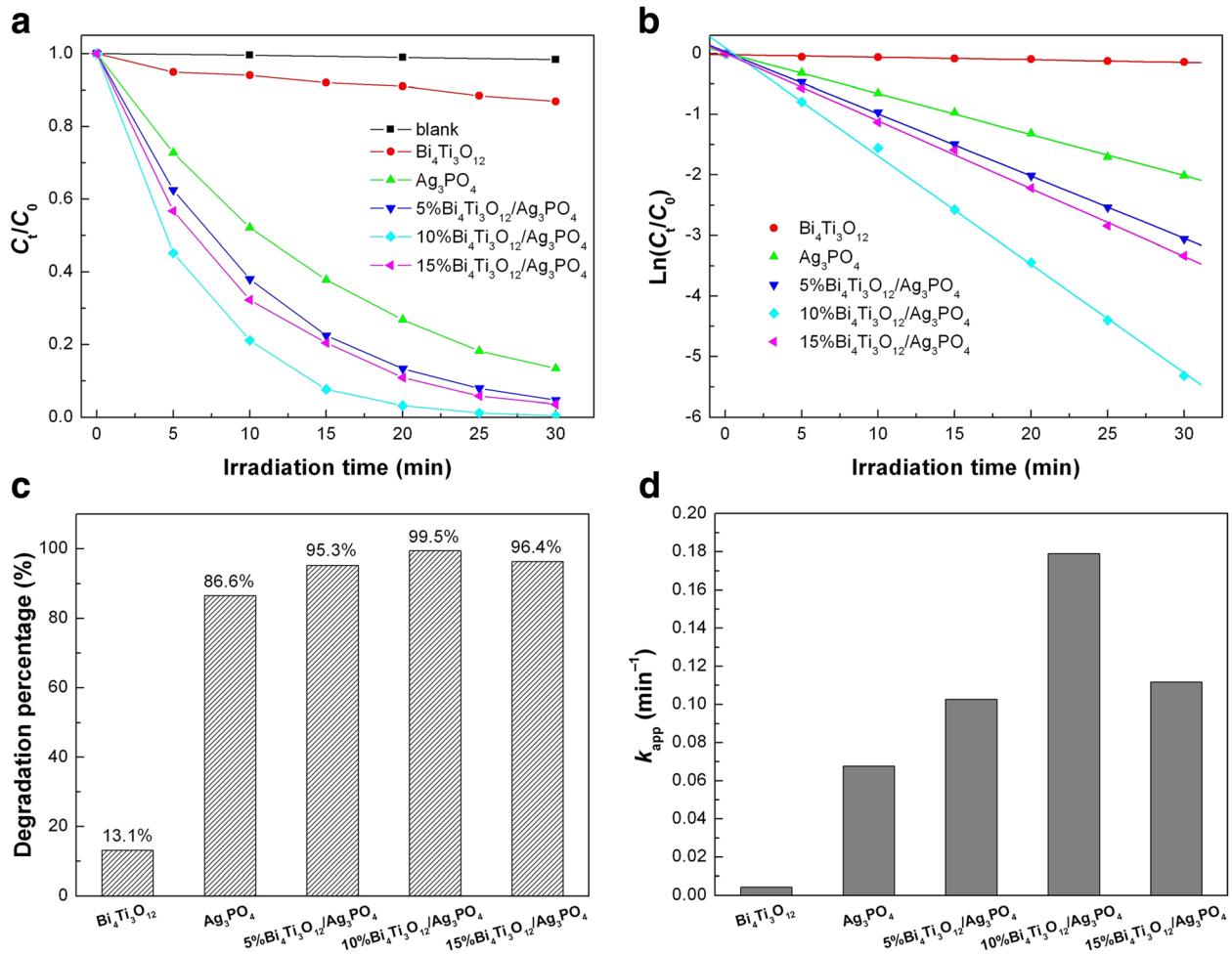

Fig. 9 **a** Time-dependent photocatalytic degradation of RhB over $Bi_4Ti_3O_{12}$, Ag_3PO_4, and $Bi_4Ti_3O_{12}/Ag_3PO_4$ composites. **b** Plots of $Ln(C_t/C_0)$ versus irradiation time t for the samples. **c** Degradation percentages of RhB after 30 min of photocatalysis over the samples. **d** Apparent first-order reaction rate constants k_{app} for the samples

effect of the scavengers on the degradation of RhB over 10% $Bi_4Ti_3O_{12}/Ag_3PO_4$. The degradation percentages of RhB after 30 min of photocatalysis and the rate constants are shown in Fig. 10b. It is found that the addition of ethanol to the reaction solution has a negligible effect on the degradation of RhB, implying that •OH plays little or no role in the dye degradation. However, the addition of BQ or AO leads to an obvious suppression on the dye degradation. Particularly, only 17.9% of RhB is observed to be degraded with the addition of AO. This suggests that h^+ and $\bullet O_2^-$ are the dominant and secondary reactive species causing the dye degradation, respectively.

Information of •OH radicals

We further examine whether there are •OH radicals formed over the simulated sunlight-irradiated 10% $Bi_4Ti_3O_{12}/Ag_3PO_4$ by PL spectroscopy using TPA as the scavenger of •OH. It is known that TPA will react with •OH to produce 2-hydroxyterephthalic acid (TAOH) that can emit photoluminescence having a wavelength of 429 nm [59]. The PL emission intensity is proportional to the amount of •OH radicals. Figure 11 shows the PL spectra of the TPA solution after reaction for 30 min over 10% $Bi_4Ti_3O_{12}/Ag_3PO_4$ and P25. It is well established that •OH is easily generated over the irradiated P25 (a mixed-phase TiO_2 photocatalyst) in water solution. As a result, the TPA reaction solution shows a strong PL signal at 429 nm when P25 is used as the photocatalyst. However, when 10% $Bi_4Ti_3O_{12}/Ag_3PO_4$ is used as the photocatalyst, the TPA reaction solution is very similar to the blank TPA solution, showing no obvious PL signal at 429 nm. This indicates that no •OH radicals are produced in the 10% $Bi_4Ti_3O_{12}/Ag_3PO_4$ photocatalytic system.

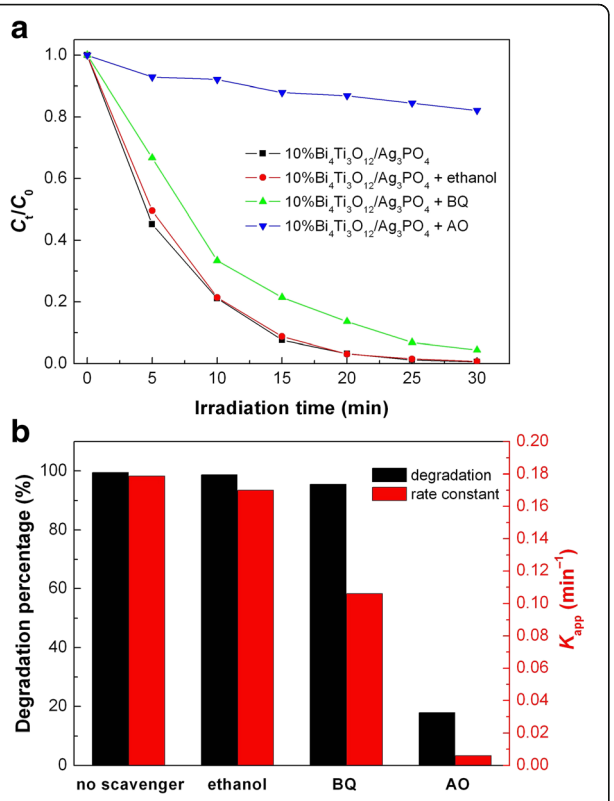

Fig. 10 Effect of ethanol, BQ, and AO on the RhB degradation over 10% $Bi_4Ti_3O_{12}/Ag_3PO_4$. **a** Time-dependent photocatalytic degradation of RhB. **b** Degradation percentages of RhB after 30 min of photocatalysis and first-order reaction rate constants k_{app}

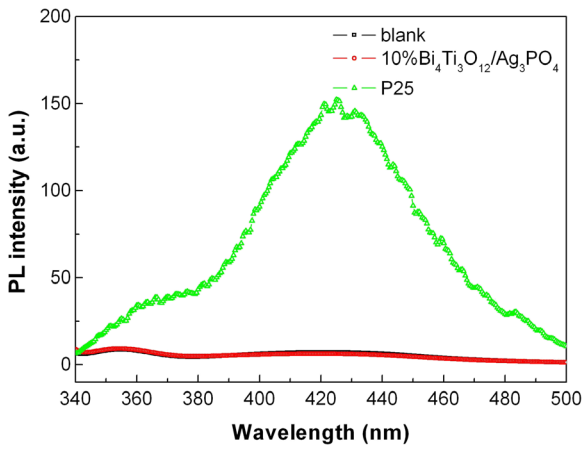

Fig. 11 PL spectra of the TPA solution reacted for 30 min over 10% $Bi_4Ti_3O_{12}/Ag_3PO_4$ and P25

Discussion of photocatalytic mechanism

The CB and VB edge potentials of $Bi_4Ti_3O_{12}$ and Ag_3PO_4 are determined according the method described in the literature [60], as schematically shown in Fig. 12a. It is seen that the CB potential of $Bi_4Ti_3O_{12}$ is negative to that of Ag_3PO_4, and moreover, $Bi_4Ti_3O_{12}$ is intrinsically an n-type semiconductor and Ag_3PO_4 behaves as a p-type semiconductor. This indicates that when the two semiconductors are integrated to form p-n heterojunction, electrons will migrate from $Bi_4Ti_3O_{12}$ to Ag_3PO_4, leaving behind positive charge centers at the interface of $Bi_4Ti_3O_{12}$ and negative charge centers at the interface of Ag_3PO_4. Simultaneously, an internal electric field is created at the interface region of the $Bi_4Ti_3O_{12}/Ag_3PO_4$ heterojunction, as shown in Fig. 12b. The direction of the internal electric field is from $Bi_4Ti_3O_{12}$ to Ag_3PO_4. Under the action of the internal electric field, photogenerated electrons will migrate from Ag_3PO_4 to $Bi_4Ti_3O_{12}$ and conversely the photogenerated holes will migrate from $Bi_4Ti_3O_{12}$ to Ag_3PO_4. Due to the carrier transfer process, the recombination of electron-hole pairs can be effectively inhibited. As a result, more photogenerated holes and electrons are able to participate in the photocatalytic reactions, thus leading to an increased photocatalytic performance of the $Bi_4Ti_3O_{12}/Ag_3PO_4$ heterojunction composites. It is noted that the photocatalytic performance of the composite photocatalysts is highly associated with

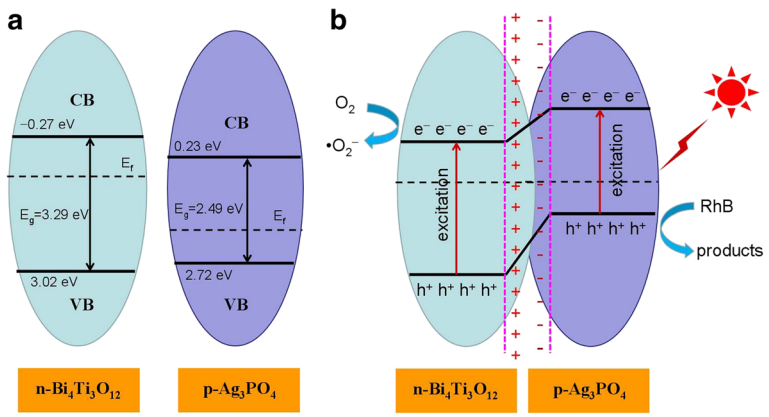

Fig. 12 Schematic illustration of the energy band structures for **a** separate $Bi_4Ti_3O_{12}$ and Ag_3PO_4 and **b** $Bi_4Ti_3O_{12}/Ag_3PO_4$ heterojunction

the number of formed heterostructures. Generally, a proper proportion between two semiconductors is required for the creation of a large number of heterostructures in the composites. In the $Bi_4Ti_3O_{12}/Ag_3PO_4$ composites, the optimum content of $Bi_4Ti_3O_{12}$ is about 10%, and at this $Bi_4Ti_3O_{12}$ content, the formed composite (i.e., $10\%Bi_4Ti_3O_{12}/Ag_3PO_4$) exhibits the highest photocatalytic activity.

Conclusions

$Bi_4Ti_3O_{12}/Ag_3PO_4$ heterojunction composites were prepared by an ion-exchange method. Compared to bare $Bi_4Ti_3O_{12}$ and Ag_3PO_4 particles, the as-prepared $Bi_4Ti_3O_{12}/Ag_3PO_4$ composites exhibit an enhanced photocatalytic activity toward the degradation of RhB under simulated sunlight irradiation. The highest photocatalytic activity is observed for the composite with $Bi_4Ti_3O_{12}$ fraction of 10%, which is about 2.6 times higher than that of bare Ag_3PO_4. The enhanced photocatalytic activity of the composites can be explained by the efficient separation of photogenerated electron-hole pairs due to the migration of the carriers between $Bi_4Ti_3O_{12}$ and Ag_3PO_4. As a result, more photogenerated holes and electrons are available for participation in the photocatalytic reactions. The reactive species are determined by investigating the effect of ethanol, BQ and AO on the RhB degradation, and it is concluded that h^+ is the dominant reactive species and $\bullet O_2^-$ is the secondary reactive species in the present $Bi_4Ti_3O_{12}/Ag_3PO_4$ photocatalytic system.

Abbreviations

BET: Brunauer-Emmett-Teller; CB: Conduction band; EIS: Electrochemical impedance spectroscopy; FTO: Fluorine-doped tin oxide; NMP: 1-Methyl-2-pyrrolidione; PL: Photoluminescence; PVDF: Polyvinylidene fluoride; RhB: Rhodamine B; SCE: Standard calomel electrode; SEM: Scanning electron microscopy; TEM: Transmission electron microscopy; TPA: Terephthalic acid; UV-vis DRS: Ultraviolet-visible diffuse reflectance spectroscopy; VB: Valence band; XPS: X-ray photoelectron spectroscopy; XRD: X-ray powder diffraction

Acknowledgements

This work was supported by the National Natural Science Foundation of China (grant nos. 51662027 and 51262018).

Authors' contributions

HY conceived the idea of experiments. CZ and ZC carried out the preparation and characterization of the samples. HY, CZ, ZC, HZ, and XW analyzed and discussed the results of the experiments. CZ wrote the manuscript, and HY amended the manuscript. All authors read and approved the final manuscript.

Authors' information

HY is a professor and a Ph.D. degree holder specializing in the investigation of photocatalytic and nanometer materials. XW is an associate professor and a Ph.D. degree holder specializing in the investigation of optical materials. HZ is an associate professor and a Ph.D. degree holder specializing in the investigation of nanometer materials. CZ and ZC are graduate students major in the study of photocatalytic materials.

Competing interests

The authors declare that they have no competing interests.

Publisher's Note

Received: 31 August 2017 Accepted: 18 November 2017
Published online: 28 November 2017

References

1. Gaya UI, Abdullah AH (2008) Heterogeneous photocatalytic degradation of organic contaminants over titanium dioxide: a review of fundamentals, progress and problems. J Photoch Photobio C 39:1–12
2. Chong MN, Jin B, Chow CWK, Saint C (2010) Recent developments in photocatalytic water treatment technology: a review. Water Res 44:2997–3027
3. Han F, Kambala VSR, Srinivasan M, Rajarathnam D, Naidu R (2009) Tailored titanium dioxide photocatalysts for the degradation of organic dyes in wastewater treatment: a review. Appl Catal A 359:25–40
4. Shekofteh-Gohari M, Habibi-Yangjeh A (2017) $Fe_3O_4/ZnO/CoWO_4$ nanocomposites: novel magnetically separable visible light-driven photocatalysts with enhanced activity in degradation of different dye pollutants. Ceram Int 43:3063–3071
5. Feizpoor S, Habibi-Yangjeh A, Vadivel S (2017) Novel TiO_2/Ag_2CrO_4 nanocomposites: efficient visible-light-driven photocatalysts with n–n heterojunctions. J Photoch Photobio A 341:57–68
6. Habibi-Yangjeh A, Shekofteh-Gohari M (2017) Novel magnetic $Fe_3O_4/ZnO/NiWO_4$ nanocomposites: enhanced visible-light photocatalytic performance through p-n heterojunctions. Sep Purif Technol 184:334–346
7. Shekofteh-Gohari M, Habibi-Yangjeh A (2016) Novel magnetically separable $ZnO/AgBr/Fe_3O_4/Ag_3VO_4$ nanocomposites with tandem n–n heterojunctions as highly efficient visible-light-driven photocatalysts. RSC Adv 6:2402–2413
8. Golzad-Nonakaran B, Habibi-Yangjeh A (2016) Ternary $ZnO/AgI/Ag_2CO_3$ nanocomposites: novel visible-light-driven photocatalysts with excellent activity in degradation of different water pollutants. Mater Chem Phys 184:210–221
9. Di L, Yang H, Xian T, Chen X (2017) Enhanced photocatalytic activity of $NaBH_4$ reduced $BiFeO_3$ nanoparticles for rhodamine B decolorization. Materials 10:1118
10. Tong X, Zhou Y, Jin L, Basu K, Adhikari R, Selopal GS, Tong X, Zhao H, Sun S, Vomierod A, Wang ZM, Rosei F (2017) Heavy metal-free, near-infrared colloidal quantum dots for efficient photoelectrochemical hydrogen generation. Nano Energy 31:441–449
11. Tong X, Kong XT, Zhou Y, Navarro-Pardo F, Selopal GS, Sun S, Govorov AO, Zhao H, Wang ZM, Rosei F (2017) Near-infrared, heavy metal-free colloidal "giant" core/shell quantum dots. Adv Energy Mater 1701432. doi:10.1002/aenm.201701432
12. Yi Z, Ye J, Kikugawa N, Kako T, Ouyang S, Stuart-Williams H, Yang H, Cao J, Luo W, Li Z, Liu Y, Withers RL (2010) An orthophosphate semiconductor with photooxidation properties under visible-light irradiation. Nat Mater 9:559–564
13. Bi Y, Ouyang S, Umezawa N, Cao J, Ye J (2011) Facet effect of single-crystalline Ag_3PO_4 sub-microcrystals on photocatalytic properties. J Am Chem Soc 133:6490–6492
14. Liang Q, Ma W, Shi Y, Li Z, Yang X (2012) Hierarchical Ag_3PO_4 porous microcubes with enhanced photocatalytic properties synthesized with the assistance of trisodium citrate. CrystEngComm 14:2966–2973
15. Bi Y, Hu H, Jiao Z, Yu H, Lu G, Ye J (2012) Two-dimensional dendritic Ag_3PO_4 nanostructures and their photocatalytic properties. Phys Chem Chem Phys 14:14486–14488
16. Wang H, He L, Wang L, Hu P, Guo L, Han X, Li J (2012) Facile synthesis of Ag_3PO_4 tetrapod microcrystals with an increased percentage of exposed {110} facets and highly efficient photocatalytic properties. CrystEngComm 14:8342–8344
17. Wang WG, Cheng B, JG Y, Liu G, Fan WH (2012) Visible-light photocatalytic activity and deactivation mechanism of Ag_3PO_4 spherical particles. Chem Asian J 7:1902–1908

18. Wang J, Teng F, Chen MXJ, Song Y, Zhou X (2013) Facile synthesis of novel Ag_3PO_4 tetrapods and the {110} facets-dominated photocatalytic activity. CrystEngComm 15:39–42
19. Jiao Z, Zhang Y, Yu H, Lu G, Ye J, Bi Y (2013) Concave trisoctahedral Ag_3PO_4 microcrystals with high-index facets and enhanced photocatalytic properties. Chem Commun 49:636–638
20. HY H, Jiao ZB, HC Y, GX L, Ye JH, Bi YP (2013) Facile synthesis of tetrahedral Ag_3PO_4 submicro-crystals with enhanced photocatalytic properties. J Mater Chem A 1:2387–2390
21. Dong PY, Wang YH, Li HH, Li H, Ma XL, Han LL (2013) Shape-controllable synthesis and morphology-dependent photocatalytic properties of Ag_3PO_4 crystals. J Mater Chem A 1:4651–4656
22. TA V, Dao CD, Hoang TTT, Nguyen KT, Le GH, Dang PT, Tran HTK, Nguyen TV (2013) Highly photocatalytic activity of novel nano-sized Ag_3PO_4 for Rhodamine B degradation under visible light irradiation. Mater Lett 92:57–60
23. Katsumata H, Taniguchi M, Kaneco S, Suzuki T (2013) Photocatalytic degradation of bisphenol A by Ag_3PO_4 under visible light. Catal Commun 34:30–34
24. Amornpitoksuk P, Intarasuwan K, Suwanboon S, Baltrusaitis J (2013) Effect of phosphate salts (Na_3PO_4, Na_2HPO_4, and NaH_2PO_4) on Ag_3PO_4 morphology for photocatalytic dye degradation under visible light and toxicity of the degraded dye products. Ind Eng Chem Res 52:17369–17375
25. Yang ZM, Tian Y, Huang GF, Huang WQ, Liu YY, Jiao C, Wan Z, Yan XG, Pan AL (2014) Novel 3D flower-like Ag_3PO_4 microspheres with highly enhanced visible light photocatalytic activity. Mater Lett 116:209–211
26. Hua X, Jin YJ, Wang K, Li N, Liu HQ, Chen MD, Paul S, Zhang Y, Zhao XD, Teng F (2014) Porous Ag_3PO_4 microtubes with improved photocatalytic properties. Catal Commun 52:49–52
27. Wan J, Sun L, Fan J, Liu EZ, Hu X, Tang CN, Yin YC (2015) Facile synthesis of porous Ag_3PO_4 nanotubes for enhanced photocatalytic activity under visible light. Appl Surf Sci 355:615–622
28. Dong C, Wang J, KL W, Ling M, Xia SH, Hu Y, Li X, Ye Y, Wei XW (2016) Rhombic dodecahedral Ag_3PO_4 architectures: controllable synthesis, formation mechanism and photocatalytic activity. CrystEngComm 18:1618–1624
29. Thiyagarajan S, Singh S, Bahadur D (2016) Reusable sunlight activated photocatalyst Ag_3PO_4 and its significant antibacterial activity. Mater Chem Phys 173:385–394
30. Gunjakar JL, Jo YK, Kim IY, Lee JM, Patil SB, Pyun JC, Hwang SJ (2016) A chemical bath deposition route to facet-controlled Ag_3PO_4 thin films with improved visible light photocatalytic activity. J Solid State Chem 240:115–121
31. Zheng CX, Yang H, Yang Y (2017) Synthesis of novel coral-like Ag_3PO_4 microspheres under the aid of trisodium citrate and acetic acid. J Ceram Soc Jpn 125:141–144
32. Umezawa N, Shuxin O, Ye J (2011) Theoretical study of high photocatalytic performance of Ag_3PO_4. Phys Rev B 83:035202
33. Bi YP, Ouyang SX, Cao JY, Ye JH (2011) Facile synthesis of rhombic dodecahedral AgX/Ag_3PO_4 (X = Cl, Br, I) heterocrystals with enhanced photocatalytic properties and stabilities. Phys Chem Chem Phys 13:10071–10075
34. Li GP, Mao LQ (2012) Magnetically separable Fe_3O_4-Ag_3PO_4 sub-micrometre composite: facile synthesis, high visible light-driven photocatalytic efficiency, and good recyclability. RSC Adv 2:5108–5111
35. Zhang LL, Zhang HC, Huang H, Liu Y, Kang ZH (2012) Ag_3PO_4/SnO_2 semiconductor nanocomposites with enhanced photocatalytic activity and stability. New J Chem 36:1541–1544
36. Liu RY, PG H, Chen SW (2012) Photocatalytic activity of Ag_3PO_4 nanoparticle/TiO_2 nanobelt heterostructures. Appl Surf Sci 258:9805–9809
37. Xu YS, Zhang WD (2013) Monodispersed Ag_3PO_4 nanocrystals loaded on the surface of spherical Bi_2MoO_6 with enhanced photocatalytic performance. Dalton T 42:1094–1101
38. Kumar S, Surendar T, Baruah A, Shanker V (2013) Synthesis of a novel and stable g-C_3N_4-Ag_3PO_4 hybrid nanocomposite photocatalyst and study of the photocatalytic activity under visible light irradiation. J Mater Chem A 1:5333–5340
39. Yang ZM, Huang GF, Huang WQ, Wei JM, Yan XG, Liu YY, Jiao C, Wan Z, Pan AL (2014) Novel Ag_3PO_4/CeO_2 composite with high efficiency and stability for photocatalytic applications. J Mater Chem A 2:1750–1756
40. Guan XJ, Guo LJ (2014) Cocatalytic effect of $SrTiO_3$ on Ag_3PO_4 toward enhanced photocatalytic water oxidation. ACS Catal 4:3020–3026
41. Mohaghegh N, Rahimi E, Gholami MR (2015) $Ag_3PO_4/BiPO_4$ p-n heterojunction nanocomposite prepared in room-temperature ionic liquid medium with improved photocatalytic activity. Mat Sci Semicon Proc 39:506–514
42. Zhu CS, Zhang L, Jiang B, Zheng JT, Hu P, Li SJ, MB W, WT W (2016) Fabrication of Z-scheme Ag_3PO_4/MoS_2 composites with enhanced photocatalytic activity and stability for organic pollutant degradation. Appl Surf Sci 377:99–108
43. Chen X, Huang X, Yi Z (2014) Enhanced ethylene photodegradation performance of g-C_3N_4–Ag_3PO_4 composites with direct Z-scheme configuration. Chem Eur J 20:1–8
44. He Y, Zhang L, Teng B, Fan M (2014) New application of Z-scheme Ag_3PO_4/g-C_3N_4 composite in converting CO_2 to fuel. Environ Sci Technol 49:649–656
45. Yang X, Chen Z, Xu J, Tang H, Chen K, Jiang Y (2015) Tuning the morphology of g-C_3N_4 for improvement of Z-scheme photocatalytic water oxidation. ACS Appl Mater Interf 7:15285–15293
46. Yang X, Tang H, Xu J, Antonietti M, Shalom M (2015) Silver phosphate/graphitic carbon nitride as an efficient photocatalytic tandem system for oxygen evolution. ChemSusChem 8:1350–1358
47. Hervoches CH, Lightfoot P (1999) A variable-temperature powder neutron diffraction study of ferroelectric $Bi_4Ti_3O_{12}$. Chem Mater 11:3359–3364
48. Zhang HJ, Chen G, Li X (2009) Synthesis and visible light photocatalysis water splitting property of chromium-doped $Bi_4Ti_3O_{12}$. Solid State Ionics 180:1599–1603
49. Zhang HP, MK L, Liu S, Wang LY, Xiu ZL, Zhou YY, Qiu ZF, Zhang AY, Ma Q (2009) Preparation and photocatalytic property of perovskite $Bi_4Ti_3O_{12}$ films. Mater Chem Phys 114:716–721
50. Lin X, Guan QF, Liu TT, Zhang Y, Zou CJ (2013) Controllable synthesis and photocatalytic activity of $Bi_4Ti_3O_{12}$ particles with different morphologies. Acta Phys-Chim Sin 29:411–417
51. He H, Yin J, Li Y, Zhang Y, Qiu H, Xu J, Xu T, Wang C (2014) Size controllable synthesis of single-crystal ferroelectric $Bi_4Ti_3O_{12}$ nanosheet dominated with {001} facets toward enhanced visible-light-driven photocatalytic activities. Appl Catal B 156–157:35–43
52. Chen ZW, Jiang H, Jin WL, Shi CK (2016) Enhanced photocatalytic performance over $Bi_4Ti_3O_{12}$ nanosheets with controllable size and exposed {001} facets for Rhodamine B degradation. Appl Catal B 180:698–706
53. Qian K, Jiang ZF, Shi H, Wei W, Zhu CZ, Xie JM (2016) Constructing mesoporous $Bi_4Ti_3O_{12}$ with enhanced visible light photocatalytic activity. Mater Lett 183:303–306
54. Cui ZM, Yang H, Zhang M, Zhang HM, JY S, Li RS (2016) Adsorption and photocatalysis performance of $Bi_4Ti_3O_{12}$ nanoparticles synthesized via a polyacrylamide gel route. Mater Trans 57:1766–1770
55. Wang F, Yang H, Zhang YC (2017) Enhanced photocatalytic performance of $CuBi_2O_4$ particles decorated with Ag nanowires. Mat Sci Semicon Proc. https://doi.org/10.1016/j.mssp.2017.09.029
56. Ye YC, Yang H, Li RS, Wang XX (2017) Enhanced photocatalytic performance and mechanism of Ag-decorated $LaFeO_3$ nanoparticles. J Sol-Gel Sci Techn 82:509–518
57. Konstantinou IK, Albanis TA (2004) TiO_2-assisted photocatalytic degradation of azo dyes in aqueous solution: kinetic and mechanistic investigations: a review. Appl Catal B 49:1–14
58. Teoh WY, Scott JA, Amal R (2012) Progress in heterogeneous photocatalysis: from classical radical chemistry to engineering nanomaterials and solar reactors. J Phys Chem Lett 3:629–639
59. Zhou M, Yang H, Xian T, Li RS, Zhang HM, Wang XX (2015) Sonocatalytic degradation of RhB over $LuFeO_3$ particles under ultrasonic irradiation. J Hazard Mater 289:149–157
60. Morrison SR (1980) Electrochemistry at semiconductor and oxidized metal electrode. Plenum, NewYork